

Article

Biosynthesis, Optical and Magnetic Properties of Fe-Doped ZnO/C Nanoparticles

Omar H. Abd-Elkader ^{1,*}, Mai Nasrallah ², Lotfi Aleya ³ and Mohamed Nasrallah ⁴

¹ Department of Physics and Astronomy, College of Science, King Saud University, P.O. Box 2455, Riyadh 11451, Saudi Arabia

² Faculty of Medicine, Ain Shams University, El-Khalyfa El-Mamoun Street, Abbassia, Cairo 11774, Egypt

³ Chrono-Environnement Laboratory, UMR CNRS 6249, Bourgogne, Franche-Comté University, CEDEX, F-25030 Besançon, France

⁴ Faculty of Medicine, Ibn Sina University, Aljerif West Block (88), Khartoum 11115, Sudan

* Correspondence: omabelkader7@ksu.edu.sa

Abstract: Employing a self-combustion method supported by egg white, pure and Fe-doped ZnO/C nanoparticles successfully biosynthesized. XRD, FTIR, Raman, SEM/EDS and TEM measurements were used to characterize the pure and doped systems. The materials under investigation's optical, surface and magnetic characteristics were recognized. Only one zinc oxide crystalline phase exhibiting a hexagonal shape comparable to wurtzite was present in the systems of pure and Fe-doped ZnO/C. Due to the variation in ionic radii, doping ZnO/C system with iron ions resulted in a decrease in unit cell volume; it revealed that ions of iron had been integrated into the lattice of zinc oxides. FTIR analysis shows characteristic vibration modes related to ZnO and that of carbon groups, confirming the formation of the ZnO/C system. In a perfect match with the IR data, which represent two bands at 1120 and 1399 cm^{-1} attributed to carbon groups, the Raman analysis shows that in the freshly manufactured materials, sp^2 and disordered G and D carbon bands have both graphitized. Fe-doping of the ZnO/C system with different amounts of iron ions resulted in the change in the size and agglomeration of the particle's system. The doped ZnO/C system has a surface area smaller than that of the pure system due to the decrease in both the mean pore radius and the total pore volume. Doping the ZnO/C system with 2 and 5 mol% Fe_2O_3 resulted in optical band gaps expanding from 3.17 eV to 3.27 eV and 3.57 eV, respectively. Due to the doping with iron ions, a magnetic transition from a fully diamagnetic state to a slightly ferromagnetic state was detected.

Keywords: Fe-doped ZnO; diamagnetism; ferromagnetism; XRD; FTIR; SEM/EDS; TEM



Citation: Abd-Elkader, O.H.; Nasrallah, M.; Aleya, L.; Nasrallah, M. Biosynthesis, Optical and Magnetic Properties of Fe-Doped ZnO/C Nanoparticles. *Surfaces* **2023**, *6*, 410–429. <https://doi.org/10.3390/surfaces6040028>

Academic Editor: Gaetano Granozzi

Received: 23 August 2023

Revised: 22 September 2023

Accepted: 7 October 2023

Published: 24 October 2023



Copyright: © 2023 by the authors. Licensee MDPI, Basel, Switzerland. This article is an open access article distributed under the terms and conditions of the Creative Commons Attribution (CC BY) license (<https://creativecommons.org/licenses/by/4.0/>).

1. Introduction

Transition metal oxides (TMOs) have occupied a large part of researchers' attention, depending on their many applications in many fields. Among these oxides, zinc oxide (ZnO) was distinguished by its unique structural, morphological, optical and electronic properties. Indeed, ZnO crystallizes in two main crystal structures including hexagonal wurtzite and cubic zincblende. The most common and stable ZnO crystal is the wurtzite lattice structure. Zinc oxide also contains n-type group II–VI semiconductor compounds with an extremely large band gap energy of 3.37 eV and an incredibly high excitation binding energy of 60 meV that are normally chemically and thermally stable [1]. The different properties of zinc oxide can be controlled and controlled by various factors, including various preparation methods and the doping process.

Incorporation of small amounts of magnetic ions in the lattice of nonmagnetic semiconductors resulted in a change their band gap, light absorption and magnetic properties, with the subsequent formation of diluted magnetic semiconductors (DMSs). The diluted magnetic semiconductor is characterized by the combination of magnetic and semi-conductive properties in one material forming spintronic [2,3]. DMSs are anticipated to be desirable

materials for magnetic-based multipurpose gadgets, such as gas detectors, spinning transistors with field effects, optical technology, field-emitting equipment, quantum computation devices and Ultraviolet defenders [4–8]. Since spin-based multipurpose electronic equipment has a variety of advantages over conventional charge-based devices in the areas of information processing speed, non-volatility and greater integration densities, spintronics (or spin-based electronics) is really the topic of significant research [9,10]. There are many different ways to prepare zinc oxide, including sol–gel, precipitation, sonochemical, microwave and hydrothermal methods [11–13].

Recently, the dilute magnetic oxides (DMOs), such as ZnO- or TiO₂-based DMOs, have been the subject of numerous investigations that display dilute ferromagnetism by using a dopant agent [14]. In fact, combining magnetic materials, like Cr, Co, Fe, Ni and Mn, with zinc oxide in many cases led to the creation of a promising DMS with degrees of freedom for both charge and rotation, in which only a tiny percentage of host cations are replaced by dopant ions [15–19]. In other words, these findings could be attributed to modulating the local electronic structure of the host ZnO lattice, with subsequent modifications in its optical, surface, morphological and electromagnetic properties due to a decrease in the band gap, which helps in electron transport in device structures [15,16]. At room temperature, ferromagnetic characteristics are produced via the exchange of spins between magnetic ions behaving as a dopant and a ZnO semiconductor responding as a carrier [20]. The solubility of the dopant in ZnO, as well as the oxide's, as the ionic radius of the zinc and dopant ranging atoms become closer together, the ferromagnetic characteristics at normal temperature are enhanced. Regulation of the elevation depends on the dopant amount's appropriate solubility in zinc oxide.

Depending on an abundance of iron on Earth, it is a suitable dopant for different systems. The band gap energy was reduced by iron-based dopants, and they also encouraged in a number of systems, electron-hole pairs are split instead of recombining. These distinctive properties of iron as dopant depend on the synthesis method, morphological change of the doped material [21,22]. Contrarily, according to many different research studies, the solubility limit of iron in ZnO varies from 3 to 8 at%, depending on the growth temperature and the amount of dopant [23–26].

Out of all the preparation methods of iron-doped ZnO, we have applied the egg white-assisted combustion method because it is the most cost effective for large-scale production. Exothermic reactions are propagated along an aqueous or sol–gel medium in this process. Many factors can affect this method, including egg white (fuel) content, precursors and heat treatment, etc. One of the best features of this method is that the final product can be obtained in less than half an hour with the help of a sustainable natural product. Moreover, this method uses the least amount of energy, while avoiding the many and complex steps of many other chemical and physical methods. In fact, the egg white-mediated green synthesis also involves the isothermal evaporation of the foam that results from the addition of precursors of egg white, which results in monodisperse and tightly regulated particle size with lower production costs [27]. Indeed, due to its complete composition of the amino acid sequences' regular structural components scattered among randomly extended chain segments, egg white can be pleated into spherical forms with sizes ranging from few to many nanometers [28]. However, the egg white's gelling, foaming and emulsifying capabilities, as well as its solubility in water and its capacity to combine with metal ions, allow for the quicker creation of nanosized particles [29]. The egg white-assisted combustion method helps us to prepare ZnO nanoparticles with 19 nm within 20 min compared with the earlier work that required a long time [27,30].

The objective of this work is to physically describe the as-produced Fe-doped ZnO/C nanoparticles employing the egg white-supplied combustion mechanism. It has been shown through this research how the structural, vibrational, morphological, surface, optical and magnetic responses of nanoparticles of ZnO doped with Fe exhibit a highly accurate correlation.

2. Materials and Methods

2.1. Materials

The chemical compounds Zinc nitrate hexahydrate and Iron nitrate nonahydrate were utilized as the active ingredients. The Sigma-Aldrich Company, based in Darmstadt, Germany, provided this content. This reagent was employed quantitatively; therefore, no additional processing was required. The egg whites were obtained by extracting eggs that were freshly laid from Egyptian chicks.

2.2. Preparation Method

Three samples (S1, S2 and S3) of pure and Fe-doped ZnO/C were manufactured using the egg white-mediated combustion route. These samples were made by completely combining hydrated metal nitrates for 2.975 g of zinc and 0 or 0.162 or 0.404 g iron with 10 mL egg white in a glass beaker. The resultant mixture was initially spun at 60 °C to enable the water to evaporate in order to raise the viscosity of the components under examination. The combination converted into a gel once the temperature approached 120 °C. The resulting precursor gel was calcined in air at 300 °C for 15 min. Suddenly, an explosion appeared in one of the edges and immediately spread among the entire group, giving the impression of an incandescent combustion, and a significant volume of foam began to form; eventually, a solid that was heavy and fluffy developed. Finally, the crystalline ZnO/C NPs with traces of amorphous carbon material were produced within 20 min, with a production yield > 99%. Iron concentrations for the S1, S2 and S3 samples were 0, 2 and 5 mol% Fe₂O₃, respectively. Zinc content for the series of pure and doped samples was fixed at one mole expressed as ZnO.

2.3. Characterization of Pure and Doped System

The structural characteristics of a variety of nanoparticles were investigated using an X-ray diffractometer with a D8 BRUKER advanced diffractometer (Karlsruhe, Germany). The patterns were run at 40 kV, 40 mA and different voltages, using Cu K α radiation with a 2° min⁻¹ scanning speed. The mean crystallite size (d), dislocation density (δ) and stress (ϵ) of the synthesized zinc oxide have been determined by utilizing Equation (1) through (3), including the Scherrer equation [27]:

$$d = \frac{B\lambda}{\beta \cos \theta} \quad (1)$$

$$\delta = \frac{1}{d^2} \quad (2)$$

$$\epsilon = \frac{\beta \cos \theta}{4} \quad (3)$$

where β is the full-width half maximum (FWHM) of diffraction, θ is the Bragg's angle, and λ is the wavelength of the utilized X-ray beam, all given in the formula, together with the average crystallite size of the phase being studied, denoted by the letter d. The Scherrer constant, B, has a value of 0.89.

The Fourier-transform infrared (FTIR) spectra of several materials were measured using a PerkinElmer Spectrophotometer (type 1430). A total of 200 mg of vacuum-dried IR-grade KBr was added to each solid sample in a two-to-one ratio. Over a range of 4000–300 cm⁻¹, FTIR spectrum data were recorded. The mixture was ground for a duration of three minutes in a vibratory ball grinder before being released using a steel press with a thirteen millimeter size. The identical discs have been placed inside the dual grating spectrophotometer chamber of the Fourier spectroscopy system.

The Raman spectra of the ZnO samples were analyzed employing a Confocal RAMAN Spectroscopy system (WI Tec, Ulm, Germany), model number α 300RS. A 532 nm fiber-coupled DPSS laser with a maximum output power of 44 mW after single-mode

fiber connection was employed as the excitation source. A high-throughput lens-based spectrograph (UHTS 300, Ulm, Germany) with a 300 mm focal length and two gratings that were both blazed at 550 nm and had a 600 g/mm and 1800 g/mm spacing was subsequently employed for collecting data. The UHTS 300 spectrograph is linked to a back-illuminated CCD camera with more than 90% QE in the visible excitation applying Cryogenic cooling. Averaging 200 accumulations per spectrum in the scan range of 50 to 4000 cm^{-1} , each spectrum was recorded at an integration period of 1.09667 s.

Using a JASCO Corp. (V-570, Jersey City, NJ 07302, USA) spectrophotometer, the produced samples' UV-Vis absorption spectra (UV-Vis) were measured over the spectral range with a precision of 0.1 nm. At room temperature, all spectra were captured.

In order to scatter individual particles over a mounting system and copper grids, the samples were initially submerged in ethanol and then subjected to just a few minutes of ultrasonic processing for scanning electron microscope (SEM) and transmittance electron micrograph (TEM) imaging, respectively, utilizing the JEOL Model 1230 and JEOL JAX-840A (both from JEOL, Tokyo, Japan).

The energy dispersive X-ray evaluation (EDS) was performed using the δ -Kevev device via a model of the 2200-JED electron microscopy system (JEOL, Tokyo, Japan). The following parameters were applied: 20 kV accelerator voltage, 120 s collecting time and 6 m opening width. The Asa method, Zaf rectification and Gauss approach were employed for calculating the surface molar composition.

Employing the Brunauer–Emmett–Teller technique and surface area monitors via the Micrometrics' Gemini VII 2390 V1.03 sequence, the measured surface area (S_{BET}), total pore volume (V_{p}) and mean pore radius (\bar{r}) were computed for the materials as prepared. All of the samples were subsequently out-gassed twice for a period before the measurements at a reduced pressure of 10^{-5} Torr, as well as 200 °C.

Utilizing a vibrating sample magnetometer (VSM; 9600-1 LDJ, USA) via an optimal applied field of 20 KOe, the magnetization characteristics of the evaluated solids were investigated.

3. Results and Discussion

3.1. Structural Analysis

We were able to observe how iron doping the ZnO/C system influenced the structural properties of ZnO utilizing X-diffractograms, which are displayed in Figure 1. The diffraction line profiles of the first two and third specimens are shown from $2\theta = 4^\circ$ to $2\theta = 80^\circ$. The first of the S1 solid's constructed lattice planes are shown as (100), (002), (101), (102), (110), (103), (200), (112) and (004). These values of 2θ equate to 31.62° , 34.38° , 36.11° , 56.32° , 62.61° , 65.06° , 68.06° and 72.52° , respectively. These planes are consistent with the standard spectra of a hexagonal phase of wurtzite-type ZnO with P63mc space group, which was identified by the interpreting of the PDF number 5–664 we obtained. A good examination of this figure confirms the following: (i) The S1 specimen's diffraction-related peaks have a medium height and are the only peaks that are connected to the S1 specimen, and no other peaks from any other crystallized phases are present conformation of ZnO with a moderate degree of crystallinity. (ii) XRD patterns of Fe-doped samples (S2 and S3) show all diffraction peaks related to ZnO crystallites, with the absence of any peaks for another phase. Additionally, the biomimetic production of ZnO utilizing egg white and the doping with various concentrations of iron oxide caused all diffraction peaks to be shifted, and both their height as well as FWHM were varied. Indeed, 2 mol% Fe_2O_3 doping brought about a decrease in the peak height and an increase in FWHM of ZnO crystallites, as shown in the S2 sample. Opposite behavior was noticed in the case of the S3 sample treated with 5 mol% Fe_2O_3 . (iii) The capacity of our team to calculate some structural characteristics of ZnO/C as shown as in Table 1 in the three different samples was made available using the results of XRD, such as crystallite size (d), lattice constants (a and c), unit cell volume (V), dislocation density (δ), Zn–O bond length (L), atom displacement to the neighboring one along the “ c ” axis (μ) and strain (ϵ). (iv) The doping ZnO/C system with 2 mol% Fe_2O_3

prompted a progressive reduction in the crystallite size of ZnO, with a subsequent increase in the strain and dislocation density. The opposite effect was observed in the case of the doping using 5 mol% Fe₂O₃. Generally, the doping of the investigated system with 2 or 5 mol% Fe₂O₃ induced a shift of an atom to its neighboring one along the “c” axis and a rise in the lattice constants.

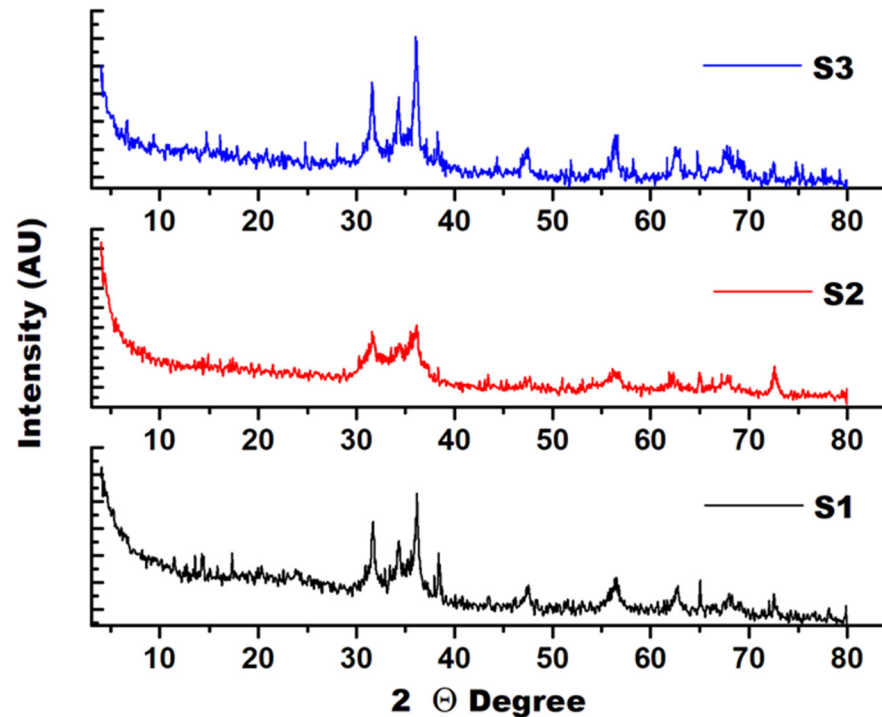


Figure 1. X-ray diffractograms of the three different specimens studied.

Table 1. Structural parameters of ZnO studied.

Structural Parameters	S1	S2	S3
d, nm	15	6	20
a, nm	0.32657	0.32737	0.32717
c, nm	0.56563	0.56702	0.56668
c/a	1.73203	1.73204	1.73206
V, nm ³	0.0655	0.0526	0.0525
μ	0.3611	0.3611	0.3611
L, nm	0.4438	0.4452	0.4448
δ, Lines/nm ²	0.0044	0.0277	0.00250
ε	0.0075	0.0184	0.0035

3.2. FTIR Analysis

To identify all of the characteristic functional groups related to these nanoparticles, qualitative chemical investigations, the three samples have been examined employing infrared spectroscopy. Figure 2 illustrates the FTIR spectra of the components as they were constructed. In the S1 samples, the metal–oxygen oscillation mode corresponds to absorbing bands within 1000 and 400 cm⁻¹, as shown from the spectrum of the FTIR. The weak bands at 620, 691 and 786 cm⁻¹ relate to the Zn–OH group, whereas the characteristic broad band at 433 cm⁻¹ is attributed to metal–oxide stretching vibrations of the Zn–O bond [27]. The vibrational modes of carbon groupings may be responsible for the bands at 1120 and 1399 cm⁻¹. Due to the capping agent in egg white, these bands are attributed to C–H, C–O and C–OH vibrations [27,31]. The strong bands at 1590 and 3339 cm⁻¹ are due to the stretching vibrations of O–H bonds, indicating the presence of moisture during the

preparation of the IR pellet [32]. As can be observed from the FTIR spectra of the S2 and S3 samples, these spectra were made up entirely of the prior bands. However, the addition of iron ions during doping caused a modest repositioning of every absorption band and a subsequent alteration in their intensities.

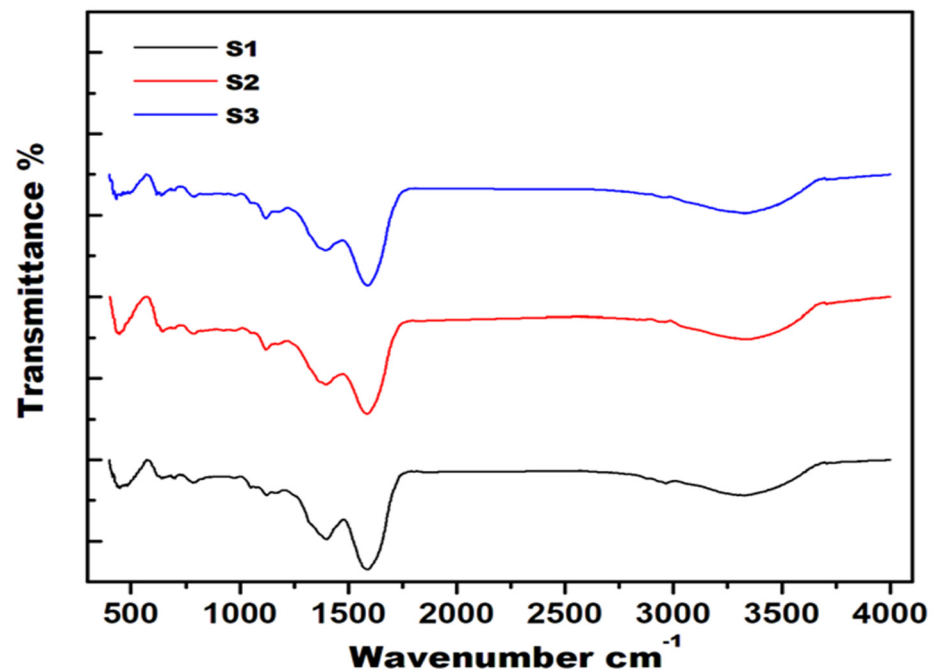


Figure 2. FTIR spectrum data for three separate samples.

3.3. Raman Analysis

Using the Raman method, the vibrational properties of three separate samples materials are investigated. Figure 3 displays the Raman spectra of the examined materials between 50 and 4000 cm^{-1} at room temperature. The Raman spectra of the S1, S2 and S3 samples did not reveal the distinctive vibrational modes connected to ZnO crystals. However, these spectra showed two large peaks in the G- and D-bands at 1565 cm^{-1} and 1326 cm^{-1} , respectively. Typical carbon compounds exhibiting these bands are a distinctive characteristic [33]. Indeed, the appearance of the G-band at 1565 cm^{-1} is a significant characteristic of sp^2 hybridized carbon materials. This band can provide specifics on the sp^2 -bonded carbon domains in-plane vibration [34]. On the other hand, the D-band occurs at 1326 cm^{-1} and indicates the existence of sp^3 defects or abnormalities inside the hexagonal graphitic structure [35]. Additionally, the edges of this band might violate the symmetry and selection criterion, be composed of amorphous carbon and hexagonal graphitic structure, or some combination of these [36]. Similar results were obtained in previous work on the preparation of ZnO nanoparticles using 5 mL egg white [27,37]. According to Ferrari and Robertson's model, the size of the crystallite is inversely proportional to the relationship (I_D/I_G) corresponding to the intensities of these bands, which is less than 2 nm for amorphous carbon [38]. In this study, the previous ratio has a small value, confirming the formation of non-crystallized carbon.

Increasing the dopant content as shown in the S3 sample resulted in an increase in the formation of amorphous carbon depending on the severe weakness in the intensities of the G- and D-bands. This finding indicates a decrease in the defect degree of carbon material. It will become clear later, when determining the surface properties, that this doping led to a significant decrease in the surface area of the S3 sample.

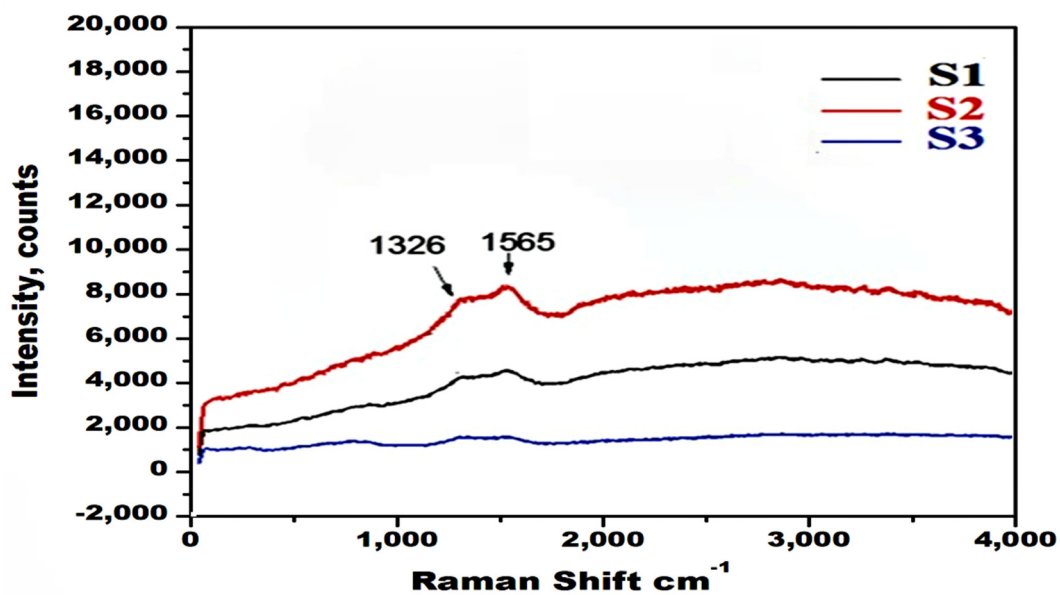


Figure 3. Vibrational Raman spectra of S1, S2 and S3 at room temperature.

3.4. Morphology and Elemental Analyses

The SEM analysis is conducted to study the morphology of the biosynthesized pure and Fe-doped ZnO/C nanoparticles. SEM images of the S1, S2 and S3 samples showed us the shape and size of the pure and doped particles, as shown as in Figure 4. These images display fragile and porous flakes containing spherical nanosized particles with the formation of various voids. In other words, the as-synthesized materials are easily broken or destroyed and also are easily crumbled or pulverized. It is worth noting that we have indicated in our previous work that this finding indicates that these chips may be carbon particles that contain zinc particles, meaning that carbon was a capping agent to help in the reduction of the size of the zinc oxide particles [27]. In this study, similar results were observed and were validated by the next EDS analysis, explained in detail in the EDS section and Figure 5. Generally, it can be seen less fragmentation of the system, yielding the largest chips. This will result in a general decrease in the system surface area. On the other hand, the increase in the content of dopant led to a slight decrease in the pores and voids due to the agglomeration of smaller nanoparticles, especially the S3 sample, which contains a high content of magnetic dopant. This indicates the possibility that this sample will have the lowest surface area, as will be shown later.

In order to have an additional and insightful look at the topography of the pure and doped ZnO/C nanoparticles, based on the identical location as that illustrated in Figure 4, the EDS evaluation of earlier samples was carried out. According to the result of the FTIR investigation, the S1 through S3 samples actually contain a minor quantity of carbonaceous material, also confirmed through the EDS results. The EDS pattern of the S1 sample displays the presence of Zn (59.39 wt%), O (13.6 wt%) and C (26.74 wt%) elements, yielding ZnO/C nanocomposite. On the other hand, EDS patterns of the S2 and S3 samples show that these samples consisted entirely of Zn (41 and 74.27 wt%, respectively), Fe (2.01 and 5.36 wt%, respectively), O (3.46 and 28.76 wt%, respectively) and C (16.88 and 28.23 wt%, respectively). An Fe-doped ZnO/C nanocomposite was produced by the S2 and S3 samples, on the other hand, as evidenced by their EDS patterns, which demonstrate that these samples were totally composed of Zn, Fe, O and C elements. The success of the creation of pure and doped ZnO/C systems is confirmed by these findings, which are in good accord with the FTIR result. Additionally, the use of gold coating to improve SEM pictures was confirmed by EDS analysis, which further supported the existence of Au.

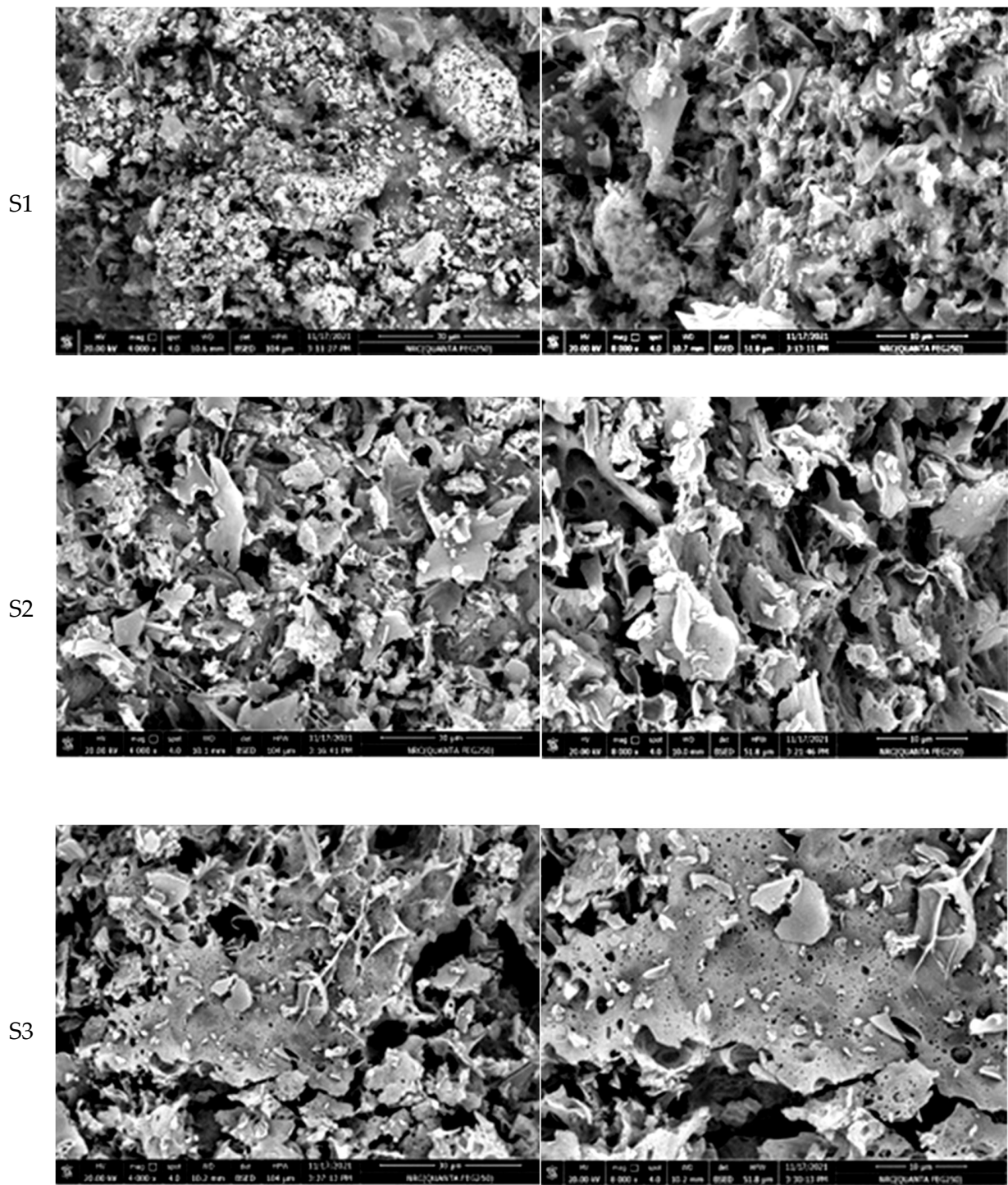


Figure 4. SEM photos of the S1 through S3 samples.

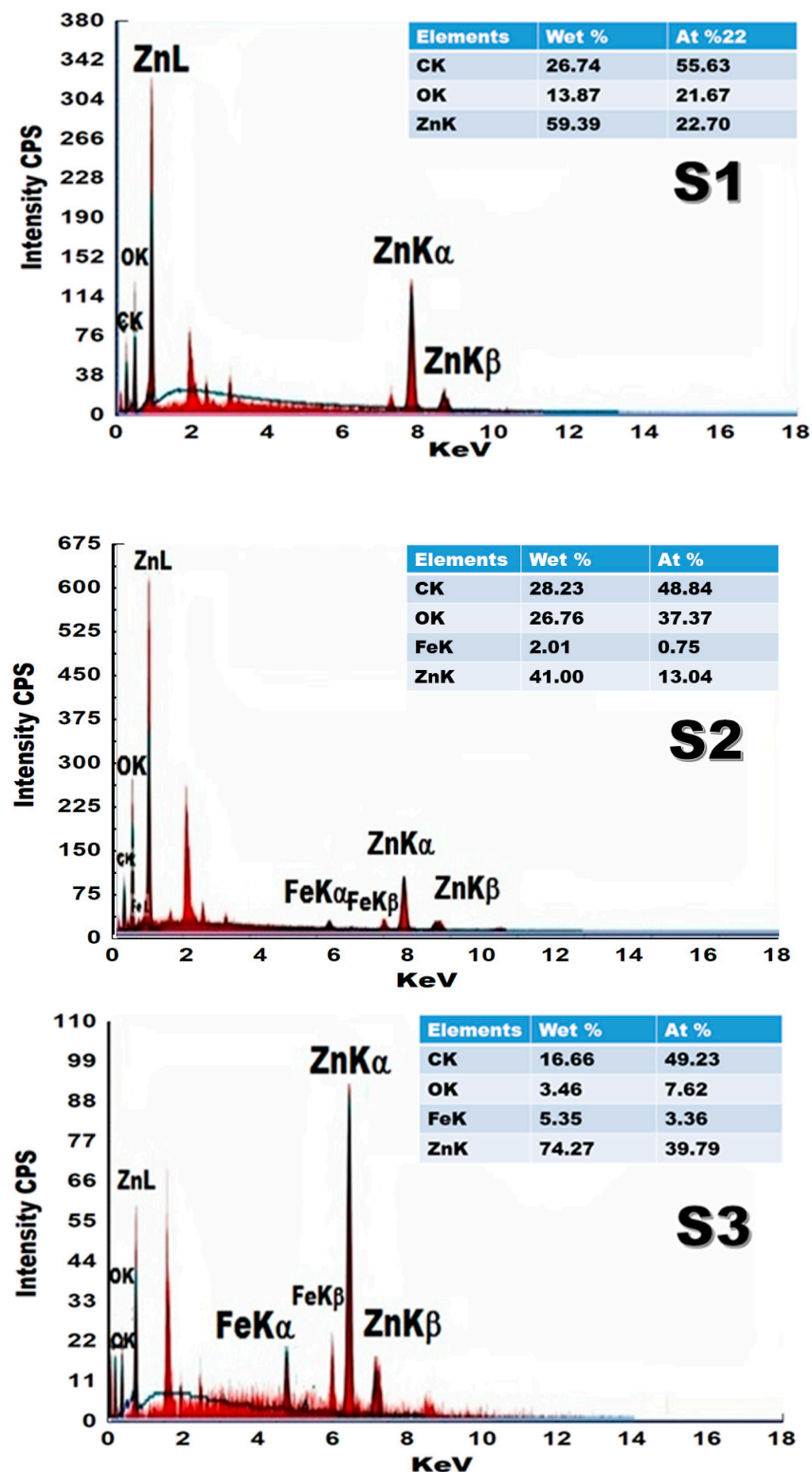


Figure 5. Energy Dispersive Spectroscopy for the samples S1 through S3.

The results of the TEM analysis confirm what was observed through the SEM analysis, with a more specific view on the nature of the pure and Fe-doped ZnO/C nanoparticles. Figure 6 displays TEM, SAED, HPSD images and histograms of the particle sizes of the S1 through S3 samples.

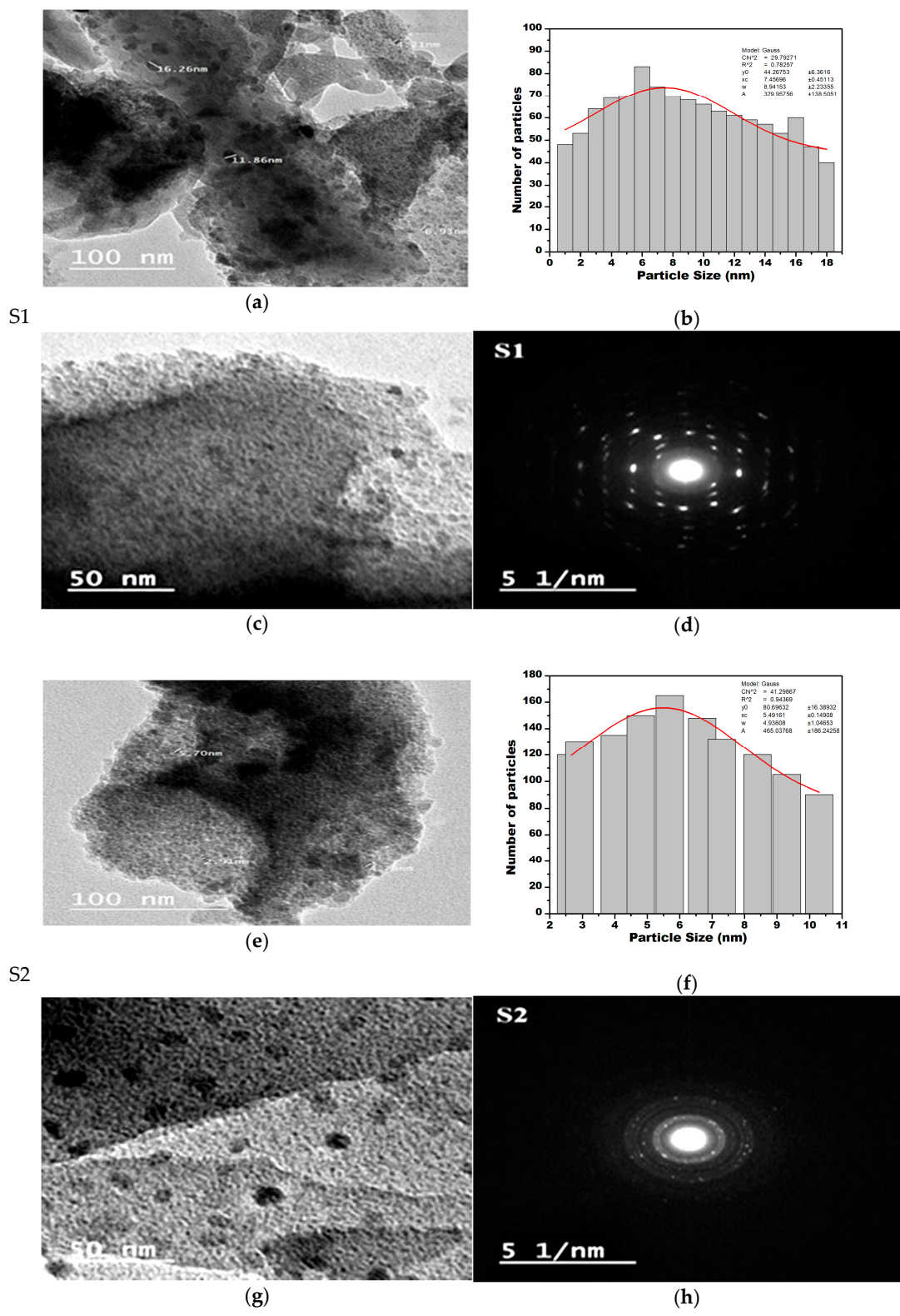


Figure 6. Cont.

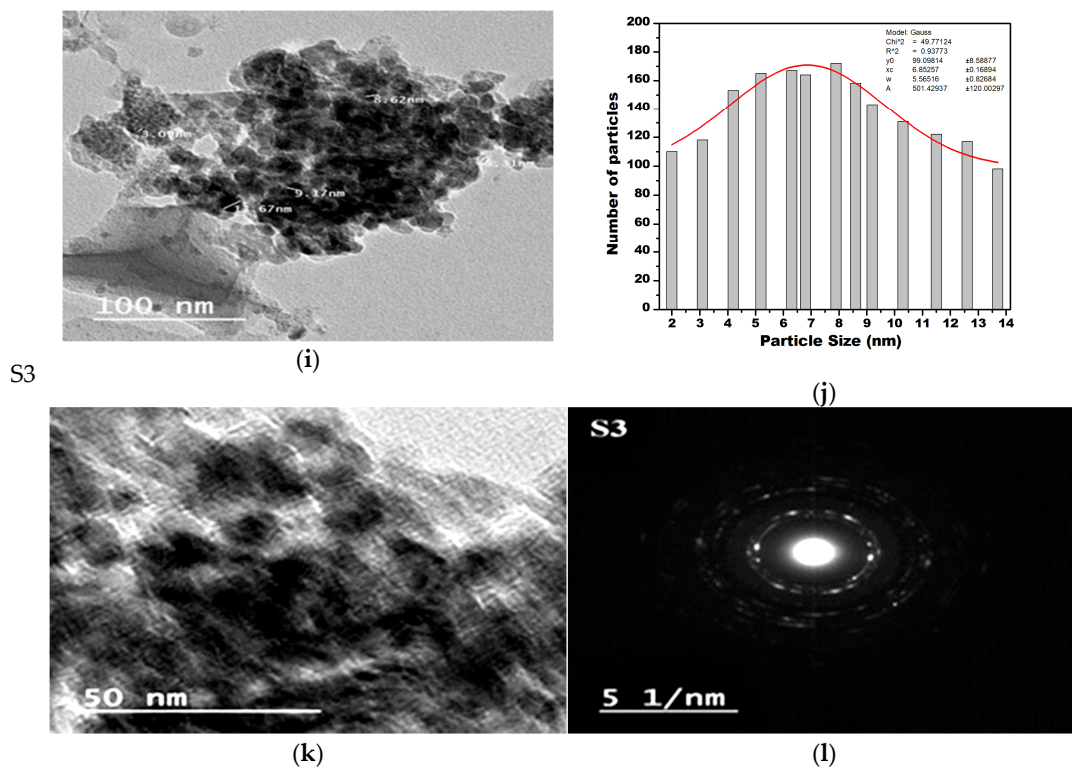


Figure 6. TEM images of the S1 through S3 samples in positions (a,c,e,g,i,k), particle size distribution histograms in position (b,f,j) and SAED in position (d,h,l).

The results of TEM agreed with SEM in that the pure and doped zinc nanoparticles are dispersed within the carbon matrix. The obvious edge in TEM images of the different samples indicated that the pure and Fe-doped ZnO/C nanoparticles were encapsulated in graphitic carbon layers. It can be seen that the S1 sample has better dispersion, depending on a decrease in the agglomeration formation rate of ZnO/C with the formation of nanoparticles [27]. The average investigated particles size of ZnO/C NPs inside the S1 sample was found to be 8 nm, as shown in the HPSD in Figure 6b,f,j. On the other hand, the doping of ZnO/C with different amounts of iron led to a slight increase in the rate of the agglomeration process, yielding some agglomerated Fe-doped ZnO/C nanoparticles, as shown in the S2 and S3 samples. Despite this simple aggregation and based on the HPSDs results in Figure 6a,c,e,g,l,k, it was found that the average size of Fe-doped ZnO/C NPs had a slight decrease and became 7 nm and 6 nm for the S2 and S3 samples, respectively. The resulting values of the size for different samples are equivalent to the estimated crystallite size calculated by the XRD technique.

The selected area electron diffraction (SAED) patterns for the manufactured samples are shown in Figure 6d,h,l. With various bright spots inside concentric rings, these patterns demonstrated the polycrystalline nature of the pure and Fe-doped ZnO/C nanoparticles. In Fe-doped ZnO/C NPs, as demonstrated in the S2 and S3 samples, the maximum intensity of these bright spots diminishes. In addition, increasing the dopant content exhibited an increase in the number of concentric rings. The authors believe that these results are due to the ZnO/C nanoparticle size reduction, with the self-aggregation of some bulk layers as a result of the dissolution of the iron particles inside them. According to XRD measurements, this dissolution causes a considerable reduction and contraction in the crystallinity of the ZnO/C lattice.

3.5. Optical Properties

The impact of Fe doping on the photophysical characteristics of ZnO/C nanoparticles was investigated on the basis of optical band gap measurements for undoped and Fe-doped samples, namely, S1 through S3. Employing diffuse reflectance measurements in the

ultraviolet–visible spectrum (UV-Vis DRS), the optical band gap for the first two and third samples was estimated. In the range of 250–2500 nm and at room temperature, Figure 7a shows the diffuse reflectance spectra of the S1, S2 and S3 samples. This image demonstrates how doping ZnO/C nanoparticles with Fe ions caused the reflectance edges to move towards lower energy wavelengths of radiation. Depending on the interpretation of the spectroscopic data using Tauc plots, as shown in Figure 7b, this shift suggests band gap expansion in the S2 and S3 samples. The optical band gap energy, E_g , of the as-prepared specimens was estimated from the Tauc equation [27,39].

$$(\alpha hv)^n = A (hv - E_g) \quad (4)$$

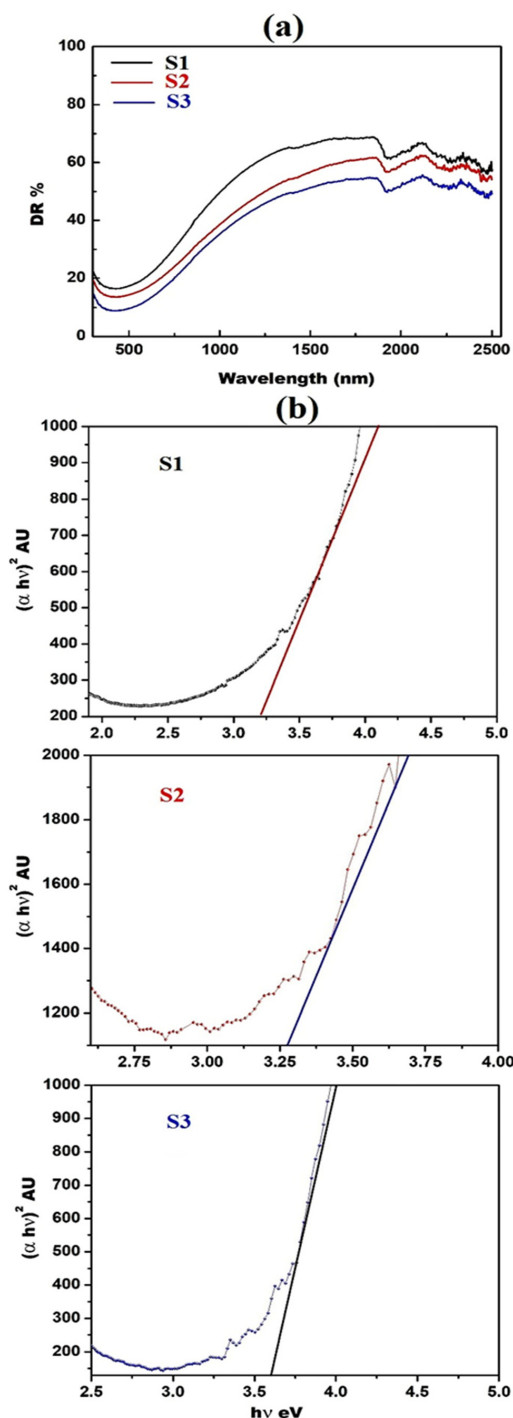


Figure 7. UV-visible spectra (a) and band gap energies (b) of the S1 through S3 samples.

Depending on the type of potential electronic transitions, n is either 2 for a direct transition or $1/2$ for an indirect transition, and other variables include the absorption coefficient (α), the proportionality constant (A), the Planck's constant (h) and the frequency of the incident photon (ν). The optical band gap value was determined by intersecting the extrapolated linear portion of a specific curve with the $(h\nu)$ axis when plotting $(\alpha h\nu)^2$ vs. photon energy ($h\nu$) for the sample under study using the Tauc equation. According to Figure 8b, the band gap energies for the S1 through S3 samples are 3.17, 3.27 and 3.57 eV, respectively. Due to the S3 sample's existence of a significant number of Fe ions, it has a greater band gap energy than the S1 sample. Actually, the presence of the most dopant caused various alterations in the band gap in semiconductor materials as a result of producing a crystal defect [40–44].

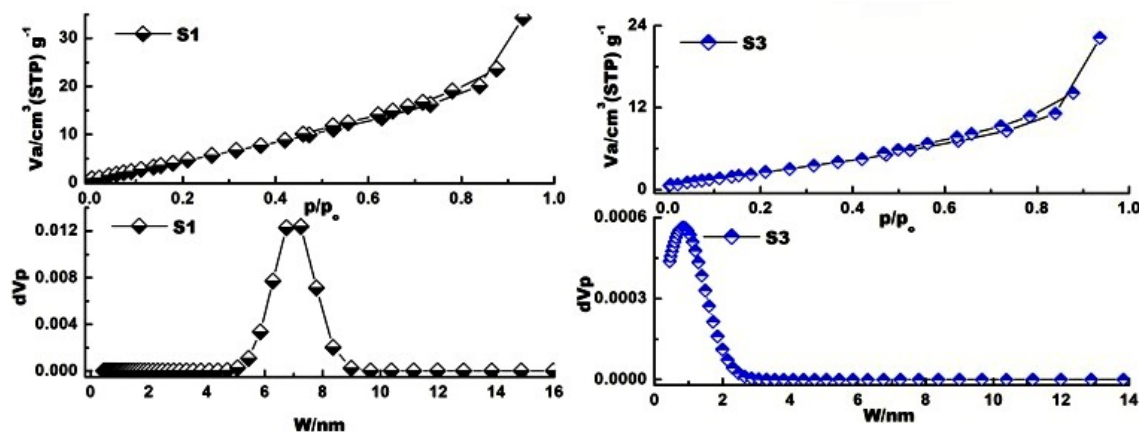


Figure 8. Pore size distribution and N_2 -adsorption isotherms of the S1 and S3 samples.

3.6. Surface Properties

Using N_2 adsorption/desorption isotherms at -196°C , the textural characteristics of the S1 and S3 samples were investigated, as shown in Figure 8. Additionally, Table 2 lists the values of various outcomes for the textural characteristics of these samples. According to IUPAC classifications, the acquired isotherms of the S1 and S3 samples conform to type-IV with a type H3 hysteresis loop [45]. This isotherm type indicates that the as-prepared solids have mesopores, depending upon the capillary condensation starting over the relative pressure $(P/P_o) = 0$.

Table 2. Surface properties of the S1 and S3 samples.

	S_{BET} m^2/g	V_m (cc/g)	\hat{r} (nm)	V_p (cc/g)
S1	29	6.73	7.23	0.053
S3	19	4.38	8.06	0.038

According to the shape of the isotherms, the adsorption process changed at high relative pressure $(P/P_o = 0.83\text{--}0.93)$, indicating the condensation process in interparticle voids. In fact, a few cavities could be seen in the SEM pictures of the S1 and S3 samples. Due to this dramatic change in the adsorption process at low relative pressure $(P/P_o = 0.05)$ with a subsequent low slope region, it is impossible to ignore the fact that our samples contain micropores. Hysteresis loops for the S1 sample have a larger area and greater variety than those for the S3 sample, showing multilayer desorption from solid pore walls. Additionally, the H3 hysteresis loop's structure reveals plate-like granules or pores with slit-like shapes. This coincides with SEM and TEM analyses that confirm the formation of sheet-like structures. According to a review of the data in Table 2, the S1 sample's S_{BET} , V_p and \hat{r} values are higher than those of the S3 sample.

The pore size distributions of the S1 and S3 samples are characterized using Non-Local Density Functional Theory (NLDFT) for nitrogen adsorption in pores. The porosity or pore size distribution of these samples is represented by histograms in Figure 8. This picture shows that the bulk of the pores in the S1 and S3 solids are mesoporous, in accordance with the observed pores, with one model distribution placed at 7 nm and 4.0864, respectively.

3.7. Magnetic Properties

At room temperature, a magnetic field in the range of 20 KOe was applied to the S1, S2 and S3 samples to measure their magnetic characteristics. After taking these data, the hysteresis loops depicted in Figure 9 were produced. This graphic demonstrates the intrinsic diamagnetism (DM) of the S1 sample or pure ZnO/C. It is interesting to note that S2 and S3 have a somewhat S-shaped hysteresis loop, which amply proves the existence of a minute signature of RTFM. As shown in Table 3, these hysteresis loops, nevertheless, enabled us to estimate the various values of the majority of the magnetic properties, including the coercive field (H_c), remanent magnetization (M_r), saturation magnetization (M_s), squareness (M_r/M_s) and anisotropy constant (K_a), for the S2 and S3 specimens. It can be seen from this table that increasing the dopant concentration resulted in an increase in the values of M_r , M_s and K_a for the investigated system. Regarding M_r/M_s and H_c values, the opposite behavior was seen. Additionally, the change in behavior from DM to RTFM could be linked to the impacts of the present iron-based doping method, which depends on the inclusion of iron ions in the crystal structure of ZnO.

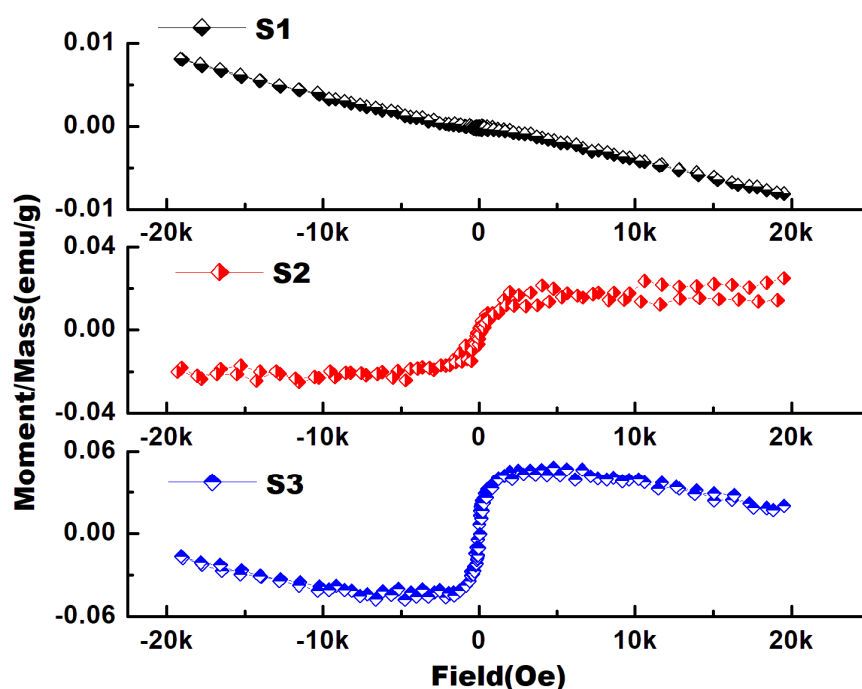


Figure 9. Room-temperature hysteresis loops of samples S1 through S3.

Table 3. Magnetic properties of S2 and S3 samples.

Samples	M_s (memu/g)	M_r (memu/g)	M_r/M_s	H_c (Oe)	K_a (erg/cm ³)
S2	9.99	8.99	0.8999	83.66	93.55
S3	41.53	12.81	0.3085	62.56	554.17

3.8. Discussion

Heating 10 mL of an egg white and zinc nitrate combination for 15 min produced pure ZnO nanoparticles having a moderate degree of crystallinity, as shown in the S1 sample.

The XRD pattern of the S1 sample consisted entirely of ZnO, without the presence of another crystalline phase. But, one cannot ignore the presence of amorphous carbon-based material as a combusted product of egg white. This was confirmed by EDS and TEM results that indicate the coexistence of carbon with zinc atoms and then the formation of the ZnO system. About the mechanism of formation of the ZnO/C system, the egg white molecules are distributed around the ZnO particles in the initial suspension. With continued good stirring, a large number of the egg white molecules are adsorbed onto the ZnO particles' surface through electrostatic attraction, forming a complex. The combustion process at 300 °C resulted in the formation of ZnO nanoparticles inside the carbon matrix yielding the ZnO/C system. By comparing this study with our previous work, we found that an increase in the amount of egg white used in the preparation of zinc oxide from 5 to 10 mL led to a clear decrease in its crystallite size, with an increase in the rest of the structural parameters, such as the lattice constants and unit cell volume [27].

On the other hand, the close-up of the (100), (002) and (101) planes of ZnO shows that the doping ZnO/C system with 2 mol% Fe₂O₃ led to a decrease in the peak height of ZnO, with an increase in the FWHM. These findings could be attributed to the smaller ionic radii of ferric ions (0.064 nm) compared to that of zinc ions (0.074 nm), while the peak height increases and FWHM decreases the doping ZnO/C system with 5 mol% Fe₂O₃ due to some agglomerations of the resulting nanoparticles, as shown in SEM and TEM results. Additionally, the ZnO crystallite sizes for the S1, S2 and S3 specimens are 15, 6 and 20 nm, respectively. The fact that the crystallite size decreased from 15 to 6 nm as a result of the 2 mol% Fe₂O₃ doping shows that iron ions were effectively incorporated into the ZnO with the restriction of its crystal lattice. But, increasing the crystallite size from 15 to 20 nm due to 5 mol% Fe₂O₃ doping indicates the formation of the agglomerate's ZnO nanoparticles, which increased their quantities by increasing the introduction of a greater amount of iron ions in the ZnO. These observations were reinforced by decreasing the unit cell volume of ZnO, depending on the smaller ionic radii of ferric ions. In addition, increasing the bond length of ZnO of the doped system studied confirms the incorporation of the most iron ions in the ZnO lattice, with the formation of some aggregates. The TEM results indicated the presence of some aggregates in the S3 sample, whose magnetism increased with the increase in iron doping. Furthermore, the deposition of the remaining carbon onto the pure and doped ZnO surface, creating the pure and Fe-doped ZnO/C combination, cannot be neglected.

Investigation of the functional groups using FTIR analysis for the S1, S2 and S3 solids indicates the presence of typical absorption bands of ZnO/C in the range of 1000–400 cm⁻¹. Additional bands at 1120 and 1399 cm⁻¹, showing the various vibration modes of various groups, including C-O, C-OH and C-H, were produced as a result of egg white-assisted green synthesis of pure and Fe-doped ZnO/C. The dwindling of the bandwidth of the pure and doped ZnO/C particles compared to that of the presence of carbon or water groups may indicate the extent of formation of this oxide in the nanoscale, depending on the presence of carbon as the capping agent and iron as the doping agent. This discovery supports the relatively low degree of crystalline nature of ZnO nanoparticles identified through XRD, SEM and TEM investigations.

The graphitization of sp² carbon (G-band) and disordered carbon (D-band), respectively, are illustrated by two peaks in the Raman spectra of pure and Fe-doped ZnO/C nanoparticles at 1565 cm⁻¹ and 1326 cm⁻¹ [37]. As a consequence of the carbonization of the as-prepared ZnO, imperfections may have been created, as seen by the shift in the intensity ratio of D vs. G. The weak peak at 1120 cm⁻¹ could be attributed to the stretching vibration of C-H at the edge of the carbon framework, according to FTIR spectra, which also showed two peaks at 1120 and 1399 cm⁻¹. The peak at 1399 cm⁻¹ could be assigned to the stretching vibration of the graphitic carbon framework.

In a previous work of some authors, they indicated the effect of zinc oxide preparation with the help of a specific quantity (5 mL) of egg white on its optical band gap energy [27]. In this study and as a continuation of our previous work, the effects of using a larger

amount of egg white (10 mL in the S1 sample), with different amounts of iron ions (2 and 5 mol% Fe₂O₃ in S2 and S3, respectively), on the optical band gap energy of ZnO were studied. In our earlier research, we discovered that the band gaps for ZnO and ZnO/C are 3.09 eV and 2.60 eV, respectively. We have pointed out that this deficiency in the gap is due to self-doping by carbon atoms produced from the combustion of egg white during the preparation method. In this study, with an increase in the amount of egg white from 5 mL to 10 mL, we found an increase in the optical band gap energy value (3.17 eV) compared to such a value (3.09 eV) of untreated sample or such a value (2.60 eV) of 5 mL treated sample. This increase could be attributed to the decrease in the particle size of ZnO due to an increase in the amount of carbon permeating the zinc nanoparticles. The authors believe that the carbon resulting from the combustion of this quantity (10 mL) of egg white behaves as a self-coating agent for the zinc particles and helped to reduce their aggregation. In other words, synthesis of ZnO nanoparticles using 10 mL egg white resulted in a 2.59% enhancement in its optical band gap energy. On the other hand, the doping of the S1 sample with different amounts of iron ions led to a larger increase in the optical band gap energy due to the formation of a degenerate semiconductor. Doping the S1 sample with 2 and 5 mol% Fe₂O₃ resulted in an increase in the optical band gap energy from 3.17 eV to 3.27 eV and 3.57 eV, respectively. The maximum increase (12.62%) in the band gap energy was observed in the case of the S3 sample. This improvement can be attributed to both the Burstein–Moss (B–M) effect and the reduction of the size of the as-prepared nanoparticles [46–50]. The B–M effect predicts that the optical band gap of degenerately doped semiconductors will widen when all states close to the conduction band become populated because of the relocation of an absorption edge to higher energy [50]. This effect offers the opportunity to obtain various optical qualities. When it came to indium (In)-doped zinc oxide nanoparticles, similar tendencies were seen [51]. A change of the optical absorption edge from blue-shift to red-shift is observed for the In-doped ZnO system, according to the doping concentration increases. The optical band gap energy increases as the concentration of Iron increases from 0 at% to 3 at%, then decreases using 5 at%. The Burstein–Moss effect is responsible for the blue-shift. It is believed that the merger of the donor and conduction bands of ZnO In at a high doping concentration is what caused the abrupt change in the absorption edge from blue-shift to red-shift.

The change in surface properties of solids due to the change in the structural properties could be attributed to the doping, phase transformation, contraction or expansion of particles, sintering and crystallinity of these solids [52]. On the other hand, any change in the morphology of solids resulted in some certain modifications in the surface properties due to the change in the porosity and shape of the material. TEM, XPS and X-ray absorption analyses of Co/CoN_x-C composite confirm the good integration of Co clusters and adjacent CoN_x species enhancing the reduction reactions (ORRs) performance in alkaline solution, depending on an obvious synergistic effect [53]. In this study, doping the ZnO/C system with a small amount of iron ions brought about a decrease in different surface properties of this system. The treatment of ZnO/C nanoparticles with 5 mol% Fe₂O₃ led to a decrease in their surface area. The decrease in the surface area of the doped ZnO/C nanoparticle can be attributed to a decrease in both the mean pore radius and total pore volume. The monolayer capacity (V_m), which dropped from 6.73 cc/g for the S1 sample to 4.38 cc/g for the S3 sample, supports this decline. The influence of surface morphology was further supported by SEM and TEM investigations, which revealed that the porosity of the S1 sample is higher than that of the S3 sample.

The S1 sample shows completely diamagnetic behavior, as observed from its hysteresis loop due to the absence of unpaired electrons [53]. Doping this sample with different amounts of iron ions led to preparation of the S2 and S3 samples having weakly ferromagnetic behavior. This indicates that doping of the ZnO/C system by iron ions resulted in a magnetic phase transition from diamagnetism to ferromagnetism due to eliciting a number of intrinsic defects of ZnO/C [54]. The defect profile of semiconductors depends on different factors, such as the doping, precursors and preparation route [27]. Zn interstitials,

O interstitials, Zn vacancies and O vacancies are the four different types of structural defects identified in ZnO/C [55]. The p-d hybridization between the host valence band and the incomplete 3d levels of transition metals (Fe ions) results in magnetic interactions between the localized magnetic moment of Fe³⁺ (3d⁵) ions and the host semiconductor (ZnO), which additionally contributes to the modest ferromagnetism in Fe-doped ZnO nanocrystals [56,57]. Both the bond length and bond angle between Zn²⁺ ions/dopant cations and O²⁻ anions favor the p-d hybridization that increases as the iron ions concentration increases [58–60]. In this investigation, room-temperature ferromagnetism was seen in the S2 and S3 samples as a result of the incorporation of Fe at O sites in the ZnO host lattice. Due to an increase in the Fe ions concentration, a mild ferromagnetic character became more noticeable with the S3 sample's greatest value of the coercive field (554.17 Oe) [61,62].

4. Conclusions

This study employed an egg white-assisted self-combustion approach to produce pure and Fe-doped ZnO/C systems. The information that follows is an overview of the structural, morphological, optical, surface and magnetic properties.

1. The egg white-assisted self-combustion method enabled us to prepare a pure and doped ZnO/C system containing an amorphous carbon matrix with moderate crystalline pure and doped ZnO nanoparticles having wurtzite-type hexagonal structure.
2. Doping the ZnO/C system with 2 and 5 mol% Fe₂O₃ led to a decrease and an increase in the crystallites size of the ZnO lattice, depending on the difference in the ionic radii of both Zn and Fe ions, and also on the formation of some agglomerates. In addition, this doping brought about a decrease in the unit cell volume, evidencing an incorporation of the dopant content used in the lattice of ZnO.
3. According to FTIR measurements, pure and doped ZnO/C nanoparticles were created utilizing an egg white-mediated combustion process, based on the presence of carbon groups at 1120 and 1399 cm⁻¹, as well as the typical ZnO absorption bands in the range of 1000–400 cm⁻¹. However, the S1, S2 and S3 samples' Raman spectra have two large peaks at 1565 cm⁻¹ and 1326 cm⁻¹ that are connected to the D- and G-bands of carbonaceous material, which is consistent with the findings of FTIR and XRD.
4. The Raman results display graphitization of sp² carbon (G-band) and disordered carbon (D-band) in the as-prepared materials, in perfect agreement with the IR results that contain two bands at 1120 and 1399 cm⁻¹ ascribed to carbon groups.
5. The surface characteristics of the pure and doped ZnO/C system were sensitive to the observed changes in their structural and morphological properties. The doped system has a surface area smaller than that of the pure system. The smaller surface area for the doped system was due to a decrease in the mean pore radius and total pore volume compared to the pure system.
6. The ferromagnetism manifestation of this system is indicated by the magnetization curve of pure and Fe-doped ZnO/C nanoparticles. As iron ions are incorporated into the crystal lattice of ZnO, the magnetic behavior of ZnO/C nanoparticles shifts from being entirely diamagnetic to being slightly ferromagnetic.

Author Contributions: Conceptualization, O.H.A.-E. and M.N. (Mai Nasrallah); methodology, M.N. (Mohamed Nasrallah); software, O.H.A.-E.; validation, O.H.A.-E., M.N. (Mai Nasrallah) and L.A.; formal analysis, O.H.A.-E.; investigation, M.N. (Mohamed Nasrallah); resources, O.H.A.-E.; data curation, O.H.A.-E.; writing—original draft preparation, O.H.A.-E., M.N. (Mai Nasrallah) and L.A.; writing—review and editing, O.H.A.-E. and M.N. (Mohamed Nasrallah); visualization, O.H.A.-E.; supervision, O.H.A.-E.; project administration, O.H.A.-E. and L.A.; funding acquisition, O.H.A.-E. All authors have read and agreed to the published version of the manuscript.

Funding: This work is supported by Researchers Supporting Project number (RSP2023R468), King Saud University, Riyadh, Saudi Arabia.

Institutional Review Board Statement: Not applicable.

Informed Consent Statement: Not applicable.

Data Availability Statement: The data presented in this study are available on request from the corresponding authors.

Acknowledgments: The authors would like to extend their sincere appreciation to Researchers Supporting Project number (RSP2023R468), King Saud University, Riyadh, Saudi Arabia.

Conflicts of Interest: There are no conflict of interest to declare.

References

1. Djurišić, A.B.; Chen, X.; Leung, Y.H.; Ng, A.M.C. ZnO nanostructures: Growth, properties and applications. *J. Mater. Chem.* **2012**, *22*, 6526–6535. [[CrossRef](#)]
2. Assadi, M.H.; Hanaor, D.A. Theoretical study on copper's energetics and magnetism in TiO₂ polymorphs. *J. Appl. Phys.* **2013**, *113*, 233913. [[CrossRef](#)]
3. Ogale, S.B. Dilute doping, defects, and ferromagnetism in metal oxide systems. *Adv. Mater.* **2010**, *22*, 3125–3155. [[CrossRef](#)] [[PubMed](#)]
4. Moezzi, A.; McDonagh, A.M.; Cortie, M.B. Zinc oxide particles: Synthesis, properties and applications. *J. Chem. Eng.* **2012**, *185*, 1–22. [[CrossRef](#)]
5. Chu, D.; Masuda, Y.; Ohji, T.; Kato, K. Formation and photocatalytic application of ZnO nanotubes using aqueous solution. *Langmuir* **2010**, *26*, 2811–2815. [[CrossRef](#)] [[PubMed](#)]
6. Zhang, J.; Wang, S.; Xu, M.; Wang, Y.; Zhu, B.; Zhang, S.; Huang, W.; Wu, S. Hierarchically porous ZnO architectures for gas sensor application. *Cryst. Growth Des.* **2009**, *9*, 3532–3537. [[CrossRef](#)]
7. Liu, X.J.; Zhu, X.Y.; Song, C.; Zeng, F.; Pan, F. Intrinsic and extrinsic origins of room temperature ferromagnetism in Ni-doped ZnO films. *J. Phys. D Appl. Phys.* **2009**, *42*, 035004. [[CrossRef](#)]
8. Neal, J.R.; Behan, A.J.; Ibrahim, R.M.; Blythe, H.J.; Ziese, M.; Fox, A.M.; Gehring, G.A. Room-temperature magneto-optics of ferromagnetic transition-metal-doped ZnO thin films. *Phys. Rev. Lett.* **2006**, *96*, 197208. [[CrossRef](#)]
9. Wolf, S.A.; Awschalom, D.D.; Buhrman, R.A.; Daughton, J.M.; Molnar, S.; Roukes, M.L.; Chtchelkanova, A.Y.; Treger, D.M. Spintronics: A spin-based electronics vision for the future'. *Science* **2001**, *294*, 1488–1495. [[CrossRef](#)]
10. Pearton, S.J.; Norton, D.P.; Ip, K.; Heo, Y.W.; Steiner, T. Recent progress in processing and properties of ZnO. *Superlattices Microstruct.* **2003**, *34*, 3–32. [[CrossRef](#)]
11. Kołodziejczak-Radzimska, A.; Jesionowski, T. Zinc oxide—From synthesis to application: A review. *Materials* **2014**, *7*, 2833–2881. [[CrossRef](#)]
12. Taglieri, G.; Daniele, V.; Maurizio, V.; Merlin, G.; Siligardi, C.; Capron, M.; Mondelli, C. New Eco-Friendly and Low-Energy Synthesis to Produce ZnO Nanoparticles for Real-World Scale Applications. *Nanomaterials* **2023**, *13*, 2458. [[CrossRef](#)] [[PubMed](#)]
13. Arief, S.; Usna, R.A. Synthesis and Properties of Magnetic-Luminescent Fe₃O₄@ZnO/C Nanocomposites. *J. Nanotechnol.* **2023**, *2023*, 2381623.
14. Pearton, S.J.; Norton, D.P.; Ivill, M.P.; Hebard, A.F.; Zavada, J.M.; Chen, W.M.; Buyanova, I.A. ZnO doped with transition metal ions. *IEEE Trans. Electron.* **2007**, *54*, 1040–1048. [[CrossRef](#)]
15. Kumar, K.; Chitkara, M.; Sandhu, I.S.; Mehta, D.; Kumar, S. Photocatalytic, optical and magnetic properties of Fe-doped ZnO nanoparticles prepared by chemical route. *J. Alloys Compd.* **2014**, *588*, 681–689. [[CrossRef](#)]
16. Yang, L.; Yanting, Y.; Huilian, L.; Lili, Y.; Yongjun, Z.; Yaxin, W.; Maobin, W.; Xiaoyan, L.; Lianhua, F.; Xin, C. Intrinsic ferromagnetic properties in Cr-doped ZnO diluted magnetic semiconductors. *J. Solid State Chem.* **2011**, *184*, 1273–1278.
17. Saleh, R.; Djaja, N.F.; Prakoso, S.P. The correlation between magnetic and structural properties of nanocrystalline transition metal-doped ZnO particles prepared by the co-precipitation method. *J. Alloys Compd.* **2013**, *546*, 48–56. [[CrossRef](#)]
18. Ahmed, F.; Kumar, S.; Arshi, N.; Anwar, M.S.; Koo, B.H.; Lee, C.G. Doping effects of Co²⁺ ions on structural and magnetic properties of ZnO nanoparticles. *Microelectron. Eng.* **2012**, *89*, 129–132. [[CrossRef](#)]
19. Choudhury, S.; Sain, S.; Mandal, M.K.; Pradhan, S.K.; Meikap, A.K. Microstructure characterization and electrical transport of nanocrystalline Zn_{0.90}Mn_{0.10}O semiconductors synthesized by mechanical alloying. *Mater. Res. Bull.* **2016**, *77*, 138–146. [[CrossRef](#)]
20. Fabbiyola, S.; Kennedy, L.J.; Dakhel, A.A.; Bououdina, M.; Vijaya, J.J.; Ratnaji, T. Structural, microstructural, optical and magnetic properties of Mn-doped ZnO nanostructures. *J. Mol. Struct.* **2016**, *1109*, 89–96. [[CrossRef](#)]
21. Carofiglio, M.; Barui, S.; Cauda, V.; Laurenti, M. Doped zinc oxide nanoparticles: Synthesis, characterization and potential use in nanomedicine. *Appl. Sci.* **2020**, *10*, 5194. [[CrossRef](#)] [[PubMed](#)]
22. Lavand, A.B.; Malghe, Y.S. Synthesis, characterization and visible light photocatalytic activity of carbon and iron modified ZnO. *J. King Saud Univ. Sci.* **2018**, *30*, 65–74. [[CrossRef](#)]
23. Dhiman, P.; Chand, J.; Kumar, A.; Kotnala, R.K.; Batoo, K.M.; Singh, M. Synthesis and characterization of novel Fe@ZnO nanosystem. *J. Alloys Compd.* **2013**, *578*, 235–241. [[CrossRef](#)]
24. Mustaqima, M.; Liu, C. ZnO-based nanostructures for diluted magnetic semiconductor. *Turk. J. Phys.* **2014**, *38*, 429–441. [[CrossRef](#)]

25. Beltrán, J.J.; Barrero, C.A.; Punnoose, A. Understanding the role of iron in the magnetism of Fe doped ZnO nanoparticles. *Phys. Chem. Chem. Phys.* **2015**, *17*, 15284–15296. [[CrossRef](#)] [[PubMed](#)]
26. Mishra, A.K.; Das, D. Investigation on Fe-doped ZnO nanostructures prepared by a chemical route. *Mater. Sci. Eng. B* **2010**, *171*, 5–10. [[CrossRef](#)]
27. Abd-Elkader, O.H.; Deraz, N.M.; Aleya, L. Rapid Bio-Assisted Synthesis and Magnetic Behavior of Zinc Oxide/Carbon Nanoparticles. *Crystals* **2023**, *13*, 1081. [[CrossRef](#)]
28. Lyckfeldt, O.; Brandt, J.; Lesca, S. Protein forming—A novel shaping technique for ceramics. *J. Eur. Ceram.* **2000**, *20*, 2551–2559. [[CrossRef](#)]
29. Maensiri, S.; Masingboon, C.; Boonchom, B.; Seraphin, S. A simple route to synthesize nickel ferrite (NiFe₂O₄) nanoparticles using egg white. *Scr. Mater.* **2007**, *56*, 797–800. [[CrossRef](#)]
30. Wu, L.; Wu, Y.; Wei, L.Ü. Preparation of ZnO nanorods and optical characterizations. *Phys. E Low-Dimens. Syst. Nanostruct.* **2005**, *28*, 76–82. [[CrossRef](#)]
31. Deepa, R.; Muthuraj, D.; Kumar, E.; Veeraputhiran, V. Microwave assisted synthesis of zinc oxide nanoparticles and its antimicrobial efficiency. *J. Nanosci. Nanotechnol.* **2019**, *5*, 640–641.
32. Kondawar, S.B.; Patil, P.T.; Agrawal, S. Chemical vapour sensing properties of electrospun nanofibers of polyaniline/ZnO nanocomposites. *Adv. Mater. Lett.* **2014**, *5*, 389–395. [[CrossRef](#)]
33. Zhang, R.; Fan, L.; Fang, Y.; Yang, S. Electrochemical route to the preparation of highly dispersed composites of ZnO/carbon nanotubes with significantly enhanced electrochemiluminescence from ZnO. *J. Mater. Chem.* **2008**, *18*, 4964–4970. [[CrossRef](#)]
34. Chen, C.; Cai, W.; Long, M.; Zhou, B.; Wu, Y.; Wu, D.; Feng, Y. Synthesis of visible-light responsive graphene oxide/TiO₂ composites with p/n heterojunction. *ACS Nano* **2010**, *4*, 6425–6432. [[CrossRef](#)] [[PubMed](#)]
35. Graf, D.; Molitor, F.; Ensslin, K.; Stampfer, C.; Jungen, A.; Hierold, C.; Wirtz, L. Spatially resolved Raman spectroscopy of single- and few-layer graphene. *Nano Lett.* **2007**, *7*, 238–242. [[CrossRef](#)] [[PubMed](#)]
36. Sim, L.C.; Leong, K.H.; Ibrahim, S.; Saravanan, P. Graphene oxide and Ag engulfed TiO₂ nanotube arrays for enhanced electron mobility and visible-light-driven photocatalytic performance. *J. Mater. Chem. A* **2014**, *2*, 5315–5322. [[CrossRef](#)]
37. Qian, Z.; Wang, L.; Dzakpasu, M.; Tian, Y.; Ding, D.; Chen, R.; Wang, G.; Yang, S. Spontaneous FeIII/FeII redox cycling in single-atom catalysts: Conjugation effect and electron delocalization. *IScience* **2003**, *26*, 105902. [[CrossRef](#)]
38. Ferrari, A.C.; Robertson, J. Interpretation of Raman spectra of disordered and amorphous carbon. *Phys. Rev. B* **2000**, *61*, 14095. [[CrossRef](#)]
39. Mostafa, N.Y.; Heiba, Z.K.; Ibrahim, M.M. Structure and optical properties of ZnO produced from microwave hydrothermal hydrolysis of tris (ethylenediamine) zinc nitrate complex. *J. Mol. Struct.* **2015**, *1079*, 480–485. [[CrossRef](#)]
40. Peña-García, R.; Guerra, Y.; Milani, R.; Oliveira, D.M.; Rodrigues, A.R.; Padrón-Hernández, E. The role of Y on the structural, magnetic and optical properties of Fe-doped ZnO nanoparticles synthesized by sol gel method. *J. Magn. Magn. Mater.* **2020**, *498*, 166085. [[CrossRef](#)]
41. Liu, L.; Liu, Z.; Yang, Y.; Geng, M.; Zou, Y.; Shahzad, M.B.; Dai, Y.; Qi, Y. Photocatalytic properties of Fe-doped ZnO electrospun nanofibers. *Ceram. Int.* **2018**, *44*, 19998–20005. [[CrossRef](#)]
42. Srivastava, A.; Kumar, N.; Misra, K.P.; Khare, S. Blue-light luminescence enhancement and increased band gap from calcium-doped zinc oxide nanoparticle films. *Mater. Sci. Semicond.* **2014**, *26*, 259–266. [[CrossRef](#)]
43. Chen, J.T.; Wang, J.; Zhang, F.; Zhang, G.A.; Wu, Z.G.; Yan, P.X. The effect of La doping concentration on the properties of zinc oxide films prepared by the sol–gel method. *J. Cryst. Growth* **2008**, *310*, 2627–2632. [[CrossRef](#)]
44. Franco, A., Jr.; Pessoni, H.V. Optical band-gap and dielectric behavior in Ho-doped ZnO nanoparticles. *Mater. Lett.* **2016**, *180*, 305–308. [[CrossRef](#)]
45. Sing, K.S. Reporting physisorption data for gas/solid systems with special reference to the determination of surface area and porosity (Provisional). *Pure Appl. Chem.* **1982**, *54*, 2201–2218. [[CrossRef](#)]
46. Singh, M.; Goyal, M.; Devlall, K. Size and shape effects on the band gap of semiconductor compound nanomaterials. *J. Taibah Univ. Sci.* **2018**, *12*, 470–475. [[CrossRef](#)]
47. Souza, F.L.; Lopes, K.P.; Longo, E.; Leite, E.R. The influence of the film thickness of nanostructured α -Fe₂O₃ on water photooxidation. *Phys. Chem. Chem. Phys.* **2009**, *11*, 1215–1219. [[CrossRef](#)] [[PubMed](#)]
48. Rahal, A.; Benramache, S.; Benhaoua, B. The effect of the film thickness and doping content of SnO₂: F thin films prepared by the ultrasonic spray method. *J. Semicond.* **2013**, *34*, 093003. [[CrossRef](#)]
49. Tuna, O.; Selamet, Y.; Aygun, G.; Ozyuzer, L. High quality ITO thin films grown by dc and RF sputtering without oxygen. *J. Phys. D Appl. Phys.* **2010**, *43*, 055402. [[CrossRef](#)]
50. Gahlawat, S.; Singh, J.; Yadav, A.K.; Ingole, P.P. Exploring Burstein–Moss type effects in nickel doped hematite dendrite nanostructures for enhanced photo-electrochemical water splitting. *Phys. Chem. Chem. Phys.* **2019**, *21*, 20463–20477. [[CrossRef](#)]
51. Tang, G.; Liu, H.; Zhang, W. The variation of optical band gap for ZnO: In films prepared by sol-gel technique. *Adv. Mater. Sci. Eng.* **2013**, *2013*, 348601. [[CrossRef](#)]
52. Deraz, N.M.; Shaban, S. Optimization of catalytic, surface and magnetic properties of nanocrystalline manganese ferrite. *J. Anal. Appl. Pyrolysis* **2009**, *86*, 173–179. [[CrossRef](#)]
53. Zhang, J.; Xie, Y.; Jiang, Q.; Guo, S.; Huang, J.; Xu, L.; Wang, Y.; Li, G. Facile synthesis of cobalt cluster-CoNx composites: Synergistic effect boosts electrochemical oxygen reduction. *J. Mater. Chem. A* **2022**, *10*, 16920–16927. [[CrossRef](#)]

54. Qi, B.; Ólafsson, S.; Gíslason, H.P. Vacancy defect-induced d0 ferromagnetism in undoped ZnO nanostructures: Controversial origin and challenges. *Prog. Mater. Sci.* **2017**, *90*, 45–74. [[CrossRef](#)]
55. Jindal, K.; Tomar, M.; Katiyar, R.S.; Gupta, V. Transition from diamagnetic to ferromagnetic state in laser ablated nitrogen doped ZnO thin films. *AIP Adv.* **2015**, *5*, 027117. [[CrossRef](#)]
56. Il'ves, V.G.; Sokovnin, S.Y. Structural and Magnetic Properties of Nanopowders and Coatings of Carbon-Doped Zinc Oxide Prepared by Pulsed Electron Beam Evaporation. *J. Nanotechnol.* **2017**, *2017*, 4628193. [[CrossRef](#)]
57. Srinet, G.; Sharma, S.; Guerrero-Sanchez, J.; Garcia-Diaz, R.; Ponce-Perez, R.; Siqueiros, J.M.; Herrera, O.R. Room-temperature ferromagnetism on ZnO nanoparticles doped with Cr: An experimental and theoretical analysis. *J. Alloys Compd.* **2020**, *849*, 156587. [[CrossRef](#)]
58. Gupta, S.; Choubey, R.K.; Sharma, L.K.; Ghosh, M.P.; Kar, M.; Mukherjee, S. Exploring the magnetic ground state of vanadium doped zinc sulphide. *Semicond. Sci. Technol.* **2019**, *34*, 105006. [[CrossRef](#)]
59. Morkoç, H.; Özgür, Ü. *Zinc Oxide: Fundamentals, Materials and Device Technology*; John Wiley & Sons: Hoboken, NJ, USA, 2008.
60. Roy, S.; Ghosh, M.P.; Mukherjee, S. Introducing magnetic properties in Fe-doped ZnO nanoparticles. *Appl. Phys. A* **2021**, *127*, 451. [[CrossRef](#)]
61. Wu, X.; Wei, Z.; Zhang, L.; Wang, X.; Yang, H.; Jiang, J. Optical and magnetic properties of Fe doped ZnO nanoparticles obtained by hydrothermal synthesis. *J. Nanomater.* **2014**, *2014*, 4. [[CrossRef](#)]
62. Abdel-Baset, T.A.; Fang, Y.W.; Anis, B.; Duan, C.G.; Abdel-Hafiez, M. Structural and magnetic properties of transition-metal-doped $Zn_{1-x}Fe_xO$. *Nanoscale Res. Lett.* **2016**, *11*, 115. [[CrossRef](#)] [[PubMed](#)]

Disclaimer/Publisher's Note: The statements, opinions and data contained in all publications are solely those of the individual author(s) and contributor(s) and not of MDPI and/or the editor(s). MDPI and/or the editor(s) disclaim responsibility for any injury to people or property resulting from any ideas, methods, instructions or products referred to in the content.